Available online at www.sciencedirect.com
ScienceDirect
Journal of Computational Physics 226 (2007) 2271–2288
JOURNAL OF COMPUTATIONAL PHYSICS
www.elsevier.com/locate/jcp

Computing traveltime and amplitude sensitivity kernels in finite-frequency tomography

Yue Tian [a,*], Raffaella Montelli [b], Guust Nolet [a], F.A. Dahlen [a]

[a] *Department of Geosciences, Guyot Hall, Princeton University, NJ 08544, USA*
[b] *ExxonMobil Upstream Research Company, P.O. Box 22189, GW03-940A, Houston, TX 77252-2189, USA*

Received 3 May 2007; received in revised form 9 July 2007; accepted 12 July 2007
Available online 26 July 2007

Abstract

The efficient computation of finite-frequency traveltime and amplitude sensitivity kernels for velocity and attenuation perturbations in global seismic tomography poses problems both of numerical precision and of validity of the paraxial approximation used. We investigate these aspects, using a local model parameterization in the form of a tetrahedral grid with linear interpolation in between grid nodes. The matrix coefficients of the linear inverse problem involve a volume integral of the product of the finite-frequency kernel with the basis functions that represent the linear interpolation. We use local and global tests as well as analytical expressions to test the numerical precision of the frequency and spatial quadrature. There is a trade-off between narrowing the bandpass filter and quadrature accuracy and efficiency. Using a minimum step size of 10 km for *S* waves and 30 km for *SS* waves, relative errors in the quadrature are of the order of 1% for direct waves such as *S*, and a few percent for *SS* waves, which are below data uncertainties in delay time or amplitude anomaly observations in global seismology. Larger errors may occur wherever the sensitivity extends over a large volume and the paraxial approximation breaks down at large distance from the ray. This is especially noticeable for minimax phases such as *SS* waves with periods >20 s, when kernels become hyperbolic near the reflection point and appreciable sensitivity extends over thousands of km. Errors becomes intolerable at epicentral distance near the antipode when sensitivity extends over all azimuths in the mantle. Effects of such errors may become noticeable at epicentral distances > 140°. We conclude that the paraxial approximation offers an efficient method for computing the matrix system for finite-frequency inversions in global tomography, though care should be taken near reflection points, and alternative methods are needed to compute sensitivity near the antipode.

PACS: 02.60.−x; 91.30.−f; 91.30.Ab; 91.30.Cd; 91.35.Pn

Keywords: Finite-frequency tomography; Sensitivity kernels; Fréchet kernels; Banana-doughnut kernels; Computational seismology; Numerical precision

* Corresponding author. Tel.: +1 609 258 1504; fax: +1 609 258 1274.
E-mail address: ytian@princeton.edu (Y. Tian).

0021-9991/$ - see front matter
doi:10.1016/j.jcp.2007.07.004

1. Introduction

Global tomographic studies using seismic body waves such as P and S have been so far mostly based on ray theory, a high-frequency approximation of the elastodynamic wave equation. Ray theory ignores wave scattering and wavefront healing effects, which render the traveltime anomalies dependent on the Earth structure in a 3D region around the geometrical ray, rather than limiting the sensitivity to an infinitesimally narrow ray path. Recently, Dahlen et al. [4,3] formulated efficient theories for 3D traveltime and amplitude sensitivity (or Fréchet) kernels, using the paraxial approximation and dynamic ray tracing [19] to reduce the computational effort. Dynamic ray tracing software to compute the geometrical spreading factors and second derivatives of the traveltime along the wavefront, which are the parameters needed for the computation of finite-frequency kernels, was described by [18], hereafter referred to as Paper I. This paper describes the algorithm that computes the sensitivity kernel and its projection on a basis of linear interpolation functions and analyses the numerical precision of the resulting matrix. An earlier version of the code was written by Montelli and applied in tomographic imaging of delay times [11,12,10]. We have extended the code by including the computation of finite-frequency kernels that can invert amplitude anomalies of seismic body waves in arbitrary frequency bands for both velocity and attenuation maps of the Earth's interior. In this paper we describe the computational algorithm and analyse its validity and numerical precision.

2. Overview

In finite-frequency tomography, the general form of the linear inverse problem is

$$d_i = \int_V K_i(\boldsymbol{r}) m(\boldsymbol{r})\, \mathrm{d}^3\boldsymbol{r}. \tag{1}$$

The i-th datum d_i is either an observed delay time δT_i or amplitude anomaly $\delta A_i/A_i$. The volume integral is theoretically over the entire Earth, but in practice limited to the region where $K_i(\boldsymbol{r})$ has an appreciable amplitude. The model parameter m represents a velocity perturbation $\delta c/c$ or attenuation perturbation $\delta Q^{-1}/Q^{-1}$, or both—in this paper we study single-parameter models only but the extension to multiple parameters is trivial, and does not affect the analysis of numerical precision.

We discretize the continuous system (1) to

$$\begin{aligned} m(\boldsymbol{r}) &= \sum_j m_j b_j(\boldsymbol{r}), \\ d_i &= \sum_j A_{ij} m_j, \\ A_{ij} &= \int_V K_i(\boldsymbol{r}) b_j(\boldsymbol{r})\, \mathrm{d}^3\boldsymbol{r}, \end{aligned} \tag{2}$$

where the functions $b_j(\boldsymbol{r})$ are a suitable basis—generally interpolation functions between a grid of nodes. In the following section we introduce such a basis for a tetrahedral grid and describe the algorithm to evaluate the integral in (2).

3. Numerical quadrature of the kernel equations

3.1. Model parameterization

Following Sambridge et al. [16,17] and Nolet and Montelli [14] we use an adaptive tetrahedral grid to span the Earth. Grid spacing can be adapted to local resolution determined by the data. We adopt a Delauney tetrahedralization using `qhull` software (Barber et al. [1] and http://www.qhull.org). For any given location $\boldsymbol{r}$, we locate the four vertices $\boldsymbol{r}_1, \boldsymbol{r}_2, \boldsymbol{r}_3, \boldsymbol{r}_4$ of the tetrahedron t that encloses $\boldsymbol{r}$, using the search algorithm developed by Sambridge and Gudmundsson [17] (see also Menke [9]). An explicit expression for the basis of interpolation functions $b_1^t(\boldsymbol{r}), b_2^t(\boldsymbol{r}), b_3^t(\boldsymbol{r}), b_4^t(\boldsymbol{r})$ for tetrahedron t is given by [17]

$$b_4^t(\boldsymbol{r}) = \frac{(\boldsymbol{r}-\boldsymbol{r}_1)\cdot[(\boldsymbol{r}_2-\boldsymbol{r}_1)\times(\boldsymbol{r}_3-\boldsymbol{r}_1)]}{(\boldsymbol{r}_4-\boldsymbol{r}_1)\cdot[(\boldsymbol{r}_2-\boldsymbol{r}_1)\times(\boldsymbol{r}_3-\boldsymbol{r}_1)]}, \tag{3}$$

where the expressions for $b_1^t(\boldsymbol{r}), b_2^t(\boldsymbol{r}), b_3^t(\boldsymbol{r})$ are given by an obvious permutation of the indices. We pre-compute the fixed coefficients in (3) for each tetrahedron to increase efficiency.

3.2. Sensitivity kernels

We give the expressions of the sensitivity kernel $K_i(\boldsymbol{r}_x)$ in (1) *under the paraxial approximation* for different types of data and model parameters. The paraxial approximation assumes that scatterers influencing the data are located close to the ray within the first a few Fresnel zones. This allows us to ignore the difference in excitation, impedance, reflection and transmission coefficients between scattered and direct waves. The paraxial approximation also makes it reasonable to approximate the scattering coefficient by 1, i.e., assuming a small angle between and the same wave type of incoming and scattered rays.

- For $d_i = \delta T_i$ and $m = \delta c/c$ (Dahlen et al. [4]):

$$K_i(\boldsymbol{r}_x) = K_T^c(\boldsymbol{r}_x) = -\frac{1}{2\pi c(\boldsymbol{r}_x)}\cdot\frac{\mathcal{R}_{rs}}{c_r\mathcal{R}_{xr}\mathcal{R}_{xs}}\cdot\frac{\int_0^\infty \omega^3|\dot{m}(\omega)|^2\sin[\omega\Delta T(\boldsymbol{r}_x)-\Delta\Phi(\boldsymbol{r}_x)]\,\mathrm{d}\omega}{\int_0^\infty \omega^2|\dot{m}(\omega)|^2\,\mathrm{d}\omega}. \tag{4}$$

- For $d_i = \delta A_i/A_i$ and $m = \delta c/c$ (Dahlen et al. [3]):

$$K_i(\boldsymbol{r}_x) = K_A^c(\boldsymbol{r}_x) = -\frac{1}{2\pi c(\boldsymbol{r}_x)}\cdot\frac{\mathcal{R}_{rs}}{c_r\mathcal{R}_{xr}\mathcal{R}_{xs}}\cdot\frac{\int_0^\infty \omega^2|\dot{m}(\omega)|^2\cos[\omega\Delta T(\boldsymbol{r}_x)-\Delta\Phi(\boldsymbol{r}_x)]\,\mathrm{d}\omega}{\int_0^\infty |\dot{m}(\omega)|^2\,\mathrm{d}\omega}. \tag{5}$$

- For $d_i = \delta A_i/A_i$ and $m = \delta Q^{-1}/Q^{-1}$ (Nolet [13]):

$$K_i(\boldsymbol{r}_x) = K_A^Q(\boldsymbol{r}_x) = -\frac{Q^{-1}}{4\pi c(\boldsymbol{r}_x)}\cdot\frac{\mathcal{R}_{rs}}{c_r\mathcal{R}_{xr}\mathcal{R}_{xs}}\cdot\frac{\int_0^\infty \omega^2|\dot{m}(\omega)|^2\sin[\omega\Delta T(\boldsymbol{r}_x)-\Delta\Phi(\boldsymbol{r}_x)]\,\mathrm{d}\omega}{\int_0^\infty |\dot{m}(\omega)|^2\,\mathrm{d}\omega}. \tag{6}$$

In (4)–(6), c_r is the seismic velocity at the receiver. The $\mathcal{R}_{rs}, \mathcal{R}_{xs}$ and $\mathcal{R}_{xr}$ are geometrical spreading factors, where subscripts rs, xs and xr represent the ray paths from source to receiver, source to scatterer, and receiver to scatterer, respectively. The detour time $\Delta T = T_{xs} + T_{xr} - T_{rs}$ is the extra time that the scatterer needs to arrive at the receiver. The detour time is determined with dynamic ray tracing by [19]:

$$\Delta T = \frac{1}{2}\boldsymbol{q}^{\mathrm{T}}\boldsymbol{H}\boldsymbol{q}, \tag{7}$$

where $\boldsymbol{H}$ is the Hessian matrix:

$$\boldsymbol{H} = \begin{pmatrix} H_{11} & 0 \\ 0 & H_{22} \end{pmatrix} = \begin{pmatrix} \partial^2 T/\partial q_1^2 & 0 \\ 0 & \partial^2 T/\partial q_2^2 \end{pmatrix}_{\boldsymbol{q}=\boldsymbol{0}},$$

and $\boldsymbol{q} = (q_1, q_2)^{\mathrm{T}}$ are ray centered coordinates perpendicular to the ray defining the location of the scatterer on the wavefront (Fig. 1). The ratio $\mathcal{R}_{rs}/(c_r\mathcal{R}_{xr}\mathcal{R}_{xs})$ can equally be obtained once $\boldsymbol{H}$ is computed [4]:

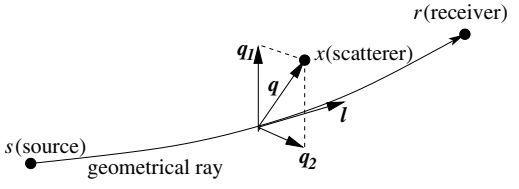

Fig. 1. Ray centered coordinates of scatterer $\boldsymbol{r}_x = (l, q_1, q_2)^{\mathrm{T}}$, where $0 \leqslant l \leqslant L$ is the length of the geometrical ray measured from source. Vectors $\boldsymbol{l}$, $\boldsymbol{q}_1$ and $\boldsymbol{q}_2$ are mutually perpendicular, with $\boldsymbol{l}$ and $\boldsymbol{q}_1$ in the source–receiver plane.

$$\frac{\mathcal{R}_{rs}}{c_r \mathcal{R}_{xs} \mathcal{R}_{xr}} = \sqrt{|\det(\boldsymbol{H})|}. \tag{8}$$

$\Delta\Phi$ is the phase shift due to passage through caustics or super critical reflection. Unless the wave is supercritically reflected with an angle-dependent phase shift, $\Delta\Phi$ takes three possible values: $0, -\pi/2, -\pi$ [4,7]. The spectrum $\dot{m}(\omega)$ in the frequency integrals is the Fourier transform of source time function $\dot{m}(t)$. We preserve the customary 'dot' notation, which reflects the fact that the observed seismic pulse is the derivative of the displacement at the fault surface. However, when the seismograms are filtered before delay times or amplitudes are measured, $\dot{m}(\omega)$ is the product of the source spectrum and the filter passband, and will usually closely resemble the shape of the filter if ω is less than the corner frequency of the source spectrum.

Computing sensitivity kernels (4)–(6) involves computing frequency integral ratios, denoted as

$$I_{p,k}[\Delta T, \dot{m}(\omega)] = \frac{\int_0^\infty \omega^p |\dot{m}(\omega)|^2 \begin{Bmatrix} \sin(\omega\Delta T) \\ \cos(\omega\Delta T) \end{Bmatrix} \mathrm{d}\omega}{\int_0^\infty \omega^{2(p-2)} |\dot{m}(\omega)|^2 \, \mathrm{d}\omega}, \tag{9}$$

which, when combined with $\sin\Delta\Phi$ and $\cos\Delta\Phi$ can express any phase shift. The power p can take the value 2 (for K_A^c and K_A^Q) or 3 (for K_T^c). $k = 1$ for a $\sin(\omega\Delta T)$ dependence, 2 for $\cos(\omega\Delta T)$. To gain efficiency, for a specific $|\dot{m}(\omega)|$, we pre-compute and store a table of $I_{p,k}$ at a set of uniformly spaced ΔT for interpolation. The spacing of ΔT is frequency-band-dependent, particularly, taken as $0.1 \times 2\pi/\omega_m$, with ω_m the highest frequency in the corresponding band.

3.3. Constructing the sensitivity matrix A_{ij}

We compute the integral in (1) by a simple Riemann sum, i.e., we split the volume into volumes ΔV_p, much smaller than the tetrahedra, around a regularly spaced grid of points $\boldsymbol{r}_p$:

$$d_i = \sum_p K_i(\boldsymbol{r}_p) m(\boldsymbol{r}_p) \Delta V_p. \tag{10}$$

To relate $m(\boldsymbol{r}_p)$ to the parameter values m_j at model nodes, we find the tetrahedron t_p that encloses $\boldsymbol{r}_p$ and interpolate:

$$m(\boldsymbol{r}_p) = \sum_{k=1}^{4} b_k^{t_p} m_k^{t_p}.$$

With this, (10) becomes

$$d_i = \sum_p K_i(\boldsymbol{r}_p) \sum_{k=1}^{4} b_k^{t_p} m_k^{t_p} \Delta V_p = \sum_p \sum_{k=1}^{4} [K_i(\boldsymbol{r}_p) b_k^{t_p} \Delta V_p] m_k^{t_p}. \tag{11}$$

To construct A_{ij} in (2) from (11), each tetrahedron vertex ($m_k^{t_p}$) is mapped back to its original parameter index (m_j), so that each volume element ΔV_p contributes to four elements of row i of matrix A_{ij}, i.e.,

$$A_{ij} \leftarrow A_{ij} + K_i(\boldsymbol{r}_p) b_k^{t_p} \Delta V_p, \quad k = 1, \ldots, 4. \tag{12}$$

Each element A_{ij} is initially set to zero and increases whenever there is contribution from the integral volume element ΔV_p, according to (12).

To construct the grid $\boldsymbol{r}_p$, we adopt ray centered coordinates $\boldsymbol{r}_x = (l, q_1, q_2)^{\mathrm{T}}$ where the $\boldsymbol{l}$-direction is along the ray path (Fig. 1). The integration is done by stepping along the ray, using a step size $\mathrm{d}l$, and define ΔV_p between two consecutive planes perpendicular to the ray (Fig. 2a and b, planes A and B). The volume element is $\Delta V_p = \mathrm{d}S\,\mathrm{d}h$, where $\mathrm{d}S$ is the surface element in plane B, and $\mathrm{d}h$ is the distance from $\boldsymbol{r}_p$ (the center of $\mathrm{d}S$) to plane A. In many cases $H_{11} \approx H_{22}$, so that the kernel cross-section is approximately circular. We therefore transform from ray centered coordinates (q_1, q_2) to polar coordinates (ρ, θ) (Fig. 2c): $\mathrm{d}S = \rho\,\mathrm{d}\rho\,\mathrm{d}\theta$, and integrate from $\rho = 0$ to ρ_m. Note that the integration step size $\mathrm{d}l$, $\mathrm{d}\rho$ has to be much smaller than the model grid spacing (see Section 3.1), to make valid the assumption in (10) that the model parameter is constant over ΔV_p.

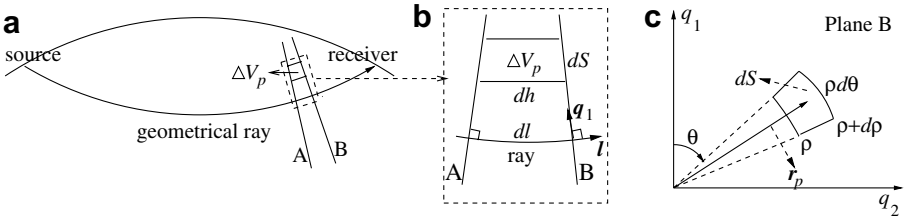

Fig. 2. The numerical scheme for kernel quadrature. (a,b) The source–receiver plane with ray centered coordinates (Fig. 1). Planes A and B are perpendicular to the ray with a distance along the ray equal to the ray tracing step size dl. $\Delta V_p = \mathrm{d}S\,\mathrm{d}h$ with dS being the surface element in plane B, and dh the distance from the center of dS to plane A. (c) Polar coordinates (ρ, θ) in plane B used for surface integration, $\mathrm{d}S = \rho\,\mathrm{d}\rho\,\mathrm{d}\theta$. Point $\boldsymbol{r}_p$ is at the center of dS.

An exception is that for surface reflected waves such as *PP*, the kernel cross-section can be hyperbolic, but the tests presented in the next section show that polar coordinates do a fairly good job for these cases.

Using (7), the largest integration radius ρ_m is defined by

$$\rho_m = \min\left(\sqrt{2\Delta T_m / \min(H_{11}, H_{22})}, \rho_{\lim}\right). \tag{13}$$

It is determined by the maximum detour time ΔT_m

$$\Delta T_m = \min(\Delta T_{xc}, \Delta T_{\lim}), \tag{14}$$

where

(1) ΔT_{xc} is the maximum length of the cross-correlation windows used to measure delay times and amplitudes;
(2) $\Delta T_{\lim}$ is the detour time for which the kernel becomes negligible, i.e., $|K(\Delta T > \Delta T_{\lim})| < \epsilon |K|_m$, where $|K|_m$ is the maximum absolute value of the kernel.

Note from (13) that ρ_m varies along the ray. The limiting radius $\rho_{\lim}$ is needed to avoid the extension of the integration beyond the limits where the paraxial approximation is still reasonably valid. Violations of the assumption of paraxiality occur when ΔT remains small for very large excursions away from the ray. Clearly, including such regions in the integration becomes meaningless. We adopted $\rho_{\lim} = 1000$ km for most of our calculations, but discuss this issue further in the next section.

Ideally, data are measured in several frequency bands, and it is efficient to define ΔT_m and ρ_m depending on frequency. For the same reason, we define the step sizes dρ and $\rho\,\mathrm{d}\theta$ to vary along the ray and with frequency, e.g.

$$\mathrm{d}\rho = \min(0.05\rho_m, \mathrm{d}\rho_0), \tag{15}$$

where dρ_0 is a constant upper limit of dρ.

3.4. Singularities at sources, receivers and caustics

At sources, receivers, and caustics of *PP*, *SS*, etc, the Hessian matrix $\boldsymbol{H}$ becomes singular ([4], Paper I), and so do sensitivity kernels (4)–(6). To avoid this, we isolate a small sphere V_0 around a singular point and apply ray theory in this sphere. The delay time due to passage through the sphere is then

$$\delta T = \int_{l\in V_0} \frac{\mathrm{d}l}{c+\delta c} - \int_{l\in V_0} \frac{\mathrm{d}l}{c} \approx -\int_{l\in V_0} \frac{1}{c}\left(\frac{\delta c}{c}\right)\mathrm{d}l, \tag{16}$$

where c is the background velocity and the line integral is along the ray path in the sphere. Comparison of (16) and (1) shows that the "ray-theoretical traveltime kernel" is $K_T^c = -c^{-1}$, and correspondingly, (12) becomes

$$A_{ij} \leftarrow A_{ij} - c^{-1}(\boldsymbol{r}_l) b_k^{tl}\,\mathrm{d}l, \quad k = 1, \ldots, 4, \tag{17}$$

where $\boldsymbol{r}_l$ represents the point on the ray in sphere V_0.

In a similar way, we can remove the singularity for K_A^Q of the attenuation anomaly $\delta Q^{-1}/Q^{-1}$. The amplitude anomaly due to passage through the sphere for a particular frequency is

$$\frac{\delta A}{A} = \frac{\exp\left(-\frac{\omega}{2}\int_{l\in V_0}\frac{Q^{-1}+\delta Q^{-1}}{c}\,\mathrm{d}l\right) - \exp\left(-\frac{\omega}{2}\int_{l\in V_0}\frac{Q^{-1}}{c}\,l\right)}{\exp\left(-\frac{\omega}{2}\int_{l\in V_0}\frac{Q^{-1}}{c}\,\mathrm{d}l\right)} \approx -\frac{\omega}{2}\int_{l\in V_0}\frac{Q^{-1}}{c}\left(\frac{\delta Q^{-1}}{Q^{-1}}\right)\mathrm{d}l. \tag{18}$$

For a wave with frequency spectrum $\dot{m}(\omega)$, following Dahlen et al. [4], it can be shown that ω in (18) should be replaced by its weighted average (Appendix A)

$$\bar{\omega} = \frac{\int_0^\infty \omega|\dot{m}(\omega)|^2\,\mathrm{d}\omega}{\int_0^\infty |\dot{m}(\omega)|^2\,\mathrm{d}\omega}. \tag{19}$$

Comparison of (18) and (1) gives the corresponding formula of (12) for the "ray-theoretical amplitude–attenuation kernel":

$$A_{ij} \leftarrow A_{ij} - \frac{\bar{\omega}Q^{-1}(\boldsymbol{r}_l)}{2c(\boldsymbol{r}_l)}\,b_k^{t_p}\,\mathrm{d}l, \quad k = 1,\ldots,4,$$

where $\boldsymbol{r}_l$ represents the point on the ray in sphere V_0.

For K_A^c, we further assume that $\delta c/c$ is constant in the sphere V_0. The assumption of homogeneous velocity perturbation is valid because V_0 is small (radius ~20 km) and we include source and receiver amplitude corrections into the unknowns to be inverted for. A constant $\delta c/c$ does not affect the ray path, and therefore leaves the amplitude unchanged (impedance effects are neglected). Therefore, in sphere V_0, the amplitude kernel $K_A^c(\boldsymbol{r}) = 0$, and model nodes ($m_j$) have no contribution to matrix A_{ij}.

Besides singularities, we also ignore the near-field effects in regions close to source or receiver, which cannot be modeled by ray-theory-based sensitivity kernels, so the kernels are less accurate in these regions [6].

3.5. Near discontinuous interfaces

We need to mirror scatterers near reflective boundaries. For reflected phases such as *PP*, *pP*, and *ScS*, a heterogeneity near the reflection point will contribute more than one scattered wave. The situation is explained in Fig. 3 for *PP*, where a scatterer near the Earth's surface produces two forward scattered waves (we neglect the backward scattering). For the first scattered wave (Fig. 3a), scatterer x sits on its incoming leg. The detour

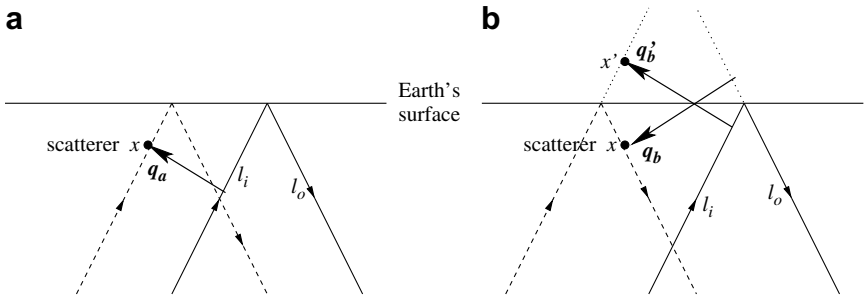

Fig. 3. The 'mirroring' procedure for scatterers near reflective boundaries, taking *PP* wave as an example. Thin solid arrows represent geometrical rays, with l_i denoting the incoming leg, and l_o the outgoing leg. Dashed arrows represent scattered rays. Dotted lines extend rays out of the reflective boundary. $\boldsymbol{q}_a$, $\boldsymbol{q}_b$, $\boldsymbol{q}_b'$ are off ray vectors in ray centered coordinates (Fig. 1). Under the paraxial approximation, there are two scattered waves from the same scatterer x near the surface reflection point: (a) x on the incoming leg of the scattered wave, (b) x on the outgoing leg of the scattered wave. x and its mirror image x' about the reflective boundary have the same detour time and geometrical spreading.

time ΔT_x is determined by Hessian matrix $\boldsymbol{H}_a$, and the scatterer's displacement $\boldsymbol{q}_a$ from the incoming leg l_i of the geometrical ray. For the second scattered wave (Fig. 3b), scatterer x sits on its outgoing leg. ΔT_x is determined by $\boldsymbol{H}_b$, evaluated at the projection of x onto the outgoing leg l_o of the geometrical ray, and $\boldsymbol{q}_b$, the scatterer's displacement from l_o. Though the projection of x onto l_o is out of the Earth, we take the mirror image x' of x about the Earth's surface. Notice $\boldsymbol{q}_b = \boldsymbol{q}'_b$, so $\Delta T_x = \Delta T_{x'}$. The above analysis for surface reflections also works for core reflections such as *ScS*.

Whenever the wavefront crosses a discontinuity, the paraxial approximation extrapolates the wavefield at the interface by maintaining the parabolic shape of the wavefront. The resultant error can only be avoided if one discards the paraxial approximation (e.g. [2]). However, the tests presented in the next section show that we are justified in ignoring this.

4. Numerical Tests

In this section we present the results of numerical tests. Since the computation of the matrix elements forms the major computational effort in seismic tomography, the trade-off between computational efficiency and numerical accuracy is an important issue.

The data we measure have large errors, typically 0.5–1 s (for global tomography) in delay times of at most a few seconds, thus the relative precision is usually worse than 10%. The errors in amplitude anomalies may even be larger, though these are still very much unknown. This means that errors of the order of a few percent in A_{ij} are acceptable.

4.1. Examples of sensitivity kernels

We first present some kernels computed for a spherically symmetric earth (IASP91), with a Gaussian source time function $\dot{m}(t)$, for which the power spectrum is [8]

$$|\dot{m}(\omega)|^2 = (\omega^2\tau^2/2\pi)\exp(-\omega^2\tau^2/4\pi^2). \tag{20}$$

Figs. 4–6 display cross-sections of the three kernels K_T^c, K_A^c, K_A^Q (see (4)–(6)) for an *S* wave observed at an epicentral distance of 60° with a dominant period of $\tau = 10$ s. The typical 'banana-doughnut' character of the kernels, with zero sensitivity (white, see Fig. 4) for delay times on the ray itself, is apparent. In fact, the attenuation kernel K_A^Q also has zero sensitivity along the geometrical ray, where K_A^c has peak sensitivity. The finite-frequency effect is strongest at the center of the ray (the doughnut is largest where the ray is deepest). Closer to the source or receiver, the doughnut is smaller but the sensitivity per km^3 is higher. For all the three kernels, the sensitivity is negative in the first Fresnel zone, which is understandable: an increase in $\delta c/c$ decreases δT; it also defocuses the wave, and thus decreases $\delta A/A$, as does an increase in attenuation $\delta Q^{-1}/Q^{-1}$. The first Fresnel zone is surrounded by a second Fresnel zone with weaker but positive sensitivity. The sensitivity becomes negligible beyond the second Fresnel zone. The typical amplitude of K_A^Q is almost three orders of magnitude less than that of K_A^c, and the difference is closer to two orders of magnitude in low Q regions like the asthenosphere. Variations of attenuation with respect to the background model may also be two orders of magnitude larger than $\delta c/c$. This can make $\delta A/A$ due to $\delta Q^{-1}/Q^{-1}$ comparable to $\delta A/A$ due to $\delta c/c$. Even so, it is clear that attenuation studies have limited validity when not combined with an estimate of the focusing involved. A similar conclusion is drawn by Ritsema et al. [15].

Figs. 7–9 display the three kernels K_T^c, K_A^c, K_A^Q (see (4)–(6)) for an *SS* wave observed at an epicentral distance of 120°, with a dominant period of $\tau = 10$ s. The *SS* wave sensitivity from source/receiver to the nearest caustic (at 40° and 80°) has a similar elliptical pattern as the *S* wave sensitivity; however, the sensitivity between two caustics has a more complex, hyperbolic pattern, because $\Delta\Phi = -\pi/2$ between the two caustics. The K_A^c cross-section between the two caustics resembles a saddle, with zero sensitivity on the asymptotes, whereas K_T^c and K_A^Q cross-sections have strongest (negative) sensitivity on the asymptotes. The aspect ratio of either the ellipse or the hyperbola becomes larger as the cross-section gets closer to the caustics, because the aspect ratio is determined by the ratio $|H_{11}/H_{22}|$, and as the cross-section approaches the caustics, $|H_{11}|$ goes to infinity with H_{22} remaining finite (Paper I). Similar plots of K_T^c and K_A^c have earlier been presented by Hung et al. [7] and Dahlen and Baig [3].

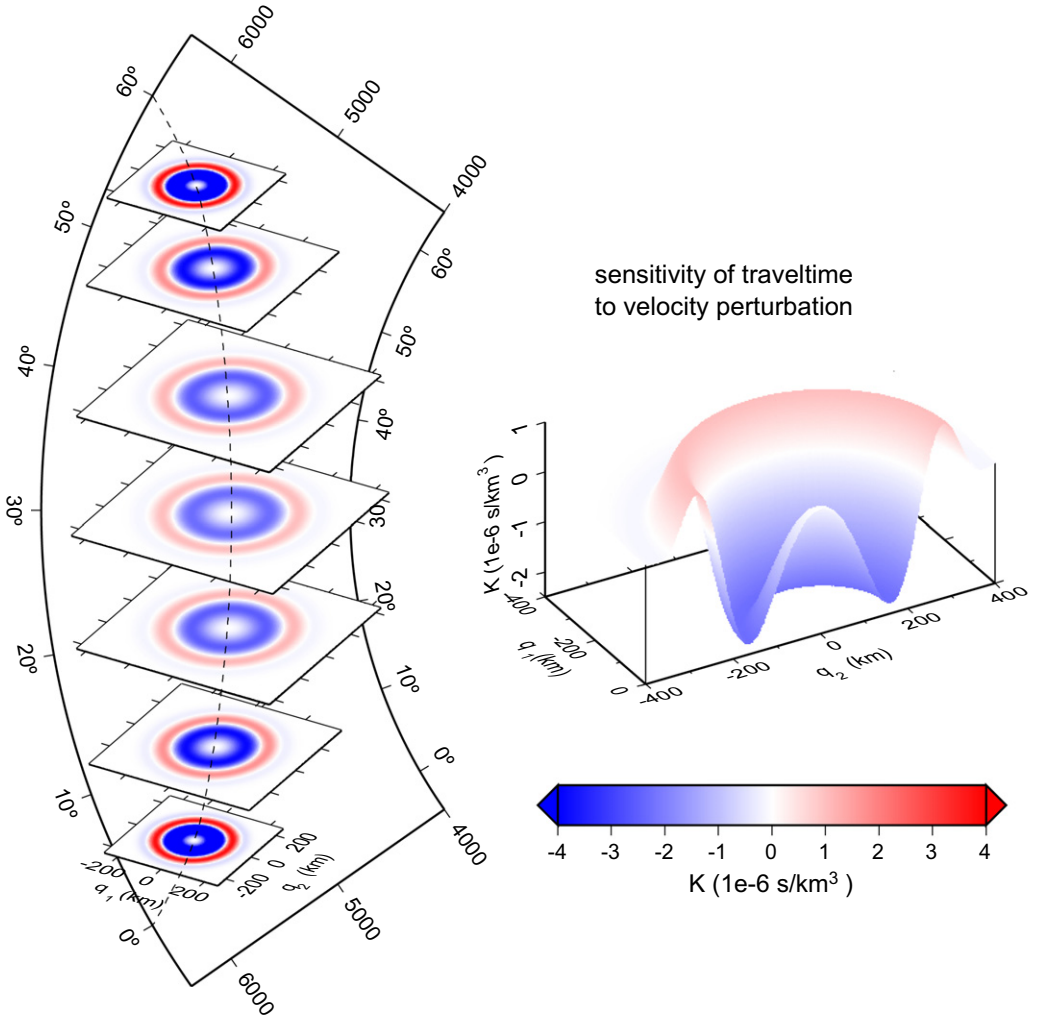

Fig. 4. Traveltime–velocity sensitivity kernel K_T^c of a 60° S wave in a spherically symmetric earth, with a dominant period of 10 s. *Left*: Dashed line is the geometrical ray. Radius (in km) and epicentral distance (in deg) are denoted. Though plotted horizontally in perspective, the planes represent cross-sections *perpendicular* to the ray at 5°, 10°, 20°, 30°, 40°, 50°, and 55° respectively, represented in ray centered coordinates (q_1, q_2) (Fig. 1). *Right*: 3D view of the cross-section at 30°. Note that only negative q_1 is plotted.

4.2. Precision of the frequency integration

We checked the precision of $I_{p,k}$ in (9) using an analytical expression for the spectrum given in (20). Favier and Chevrot [5] found

$$I_n \equiv \frac{\int_0^\infty \omega^3 |\dot{m}(\omega)|^2 \sin(\omega \Delta T)\, \mathrm{d}\omega}{\int_0^\infty \omega^2 |\dot{m}(\omega)|^2\, \mathrm{d}\omega} = \frac{8\Delta T \exp\left(-\frac{\Delta T^2 \pi^2}{\tau^2}\right) \pi^6 \left(\Delta T^4 - \frac{5\tau^2 \Delta T^2}{\pi^2} + \frac{15\tau^4}{4\pi^4}\right)}{3\tau^6} \equiv I_a.$$

We integrate over the interval $0 \leqslant \omega \leqslant \omega_{\max}$, where $|\dot{m}(\omega_{\max})| = 0.01 |\dot{m}(\omega)|_{\max}$, and use a trapezoidal rule with 40 intervals. The relative numerical error,

$$e_I = |I_n - I_a| / \max |I_a|, \tag{21}$$

shown in Fig. 10, is about 2 orders of magnitudes less than data uncertainties.

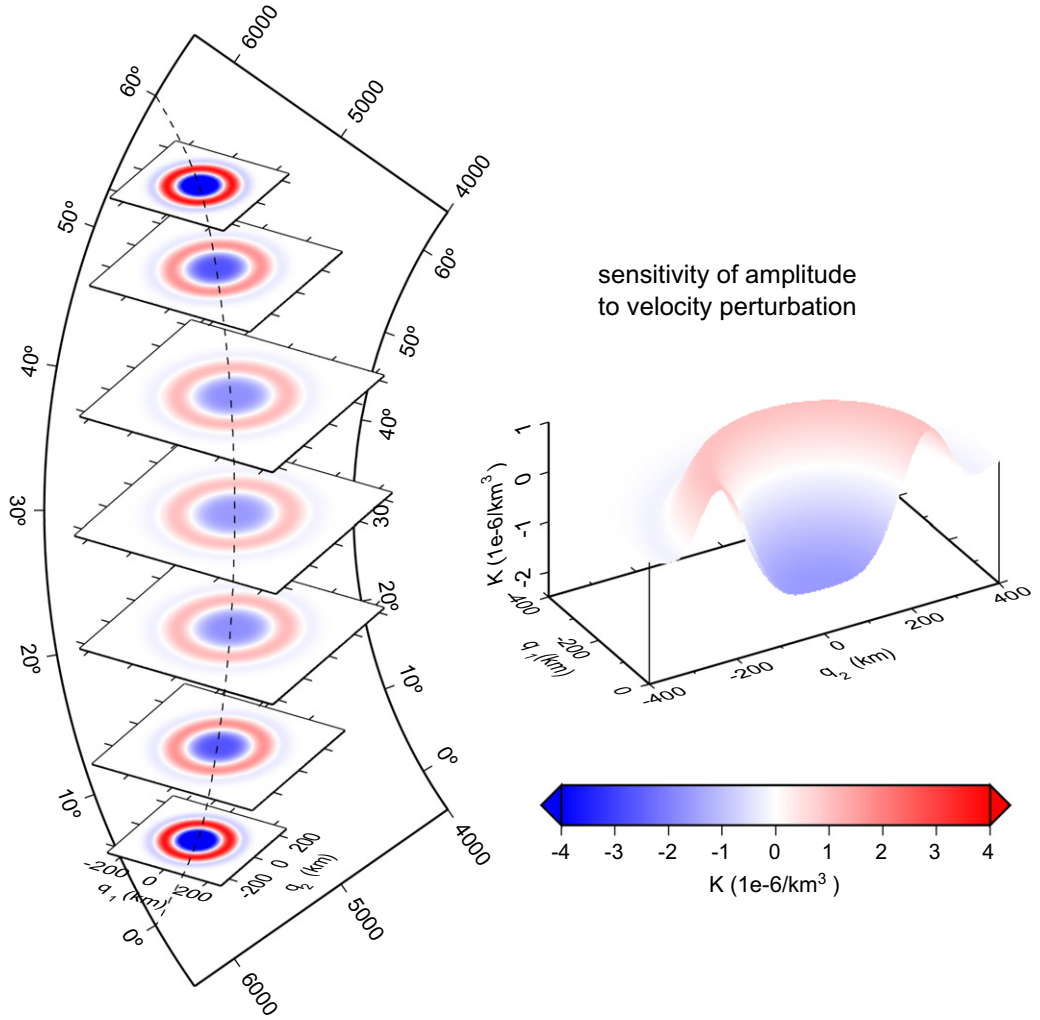

Fig. 5. Amplitude–velocity sensitivity kernel K_A^c of a 60° S wave in a spherically symmetric earth, with a dominant period of 10 sec. Notations are the same as in Fig. 4.

4.3. Influence of filters

As discussed in Section 3.2, $|\dot{m}(\omega)|$ usually closely resembles the spectra of bandpass filters used to measure the data, assuming one has an acceptable signal to noise ratio over a wide frequency band (which may not always be the case for marine seismic data). We investigate the influence of choice of filters. We compute $I_{3,1}$ in (9) for three filters with different width and shapes, but the same dominant period $\tau = 24$ s, as shown in Fig. 11. It is clear that larger and longer side lobes of $I_{3,1}$, i.e., larger higher-order Fresnel zones, occur for narrower and less smooth filters. In practice, suppressing the higher-order Fresnel zones is needed for efficiency and accuracy, because the kernel integration boundary is defined by 13,14,14, and: (1) Higher-order Fresnel zones with high sensitivity give larger $\Delta T_{\lim}$, and thus larger computation effort; (2) ρ_m is limited by the signal length ΔT_{xc}, whose typical value for $\tau = 24$ s is 50 s, which cuts through the non-zero higher-order Fresnel zones for narrow filters in 11b; (3) ρ_m is also limited by $\rho_{\lim}$, to avoid sensitivity beyond the limit of validity of the paraxial approximation, which may similarly cut through the non-zero higher-order Fresnel zones for narrow filters. Therefore, broader and smoother filters are preferred. On the other hand, filters cannot be too broad because of the need to measure data with different frequency contents. Hence, there is a

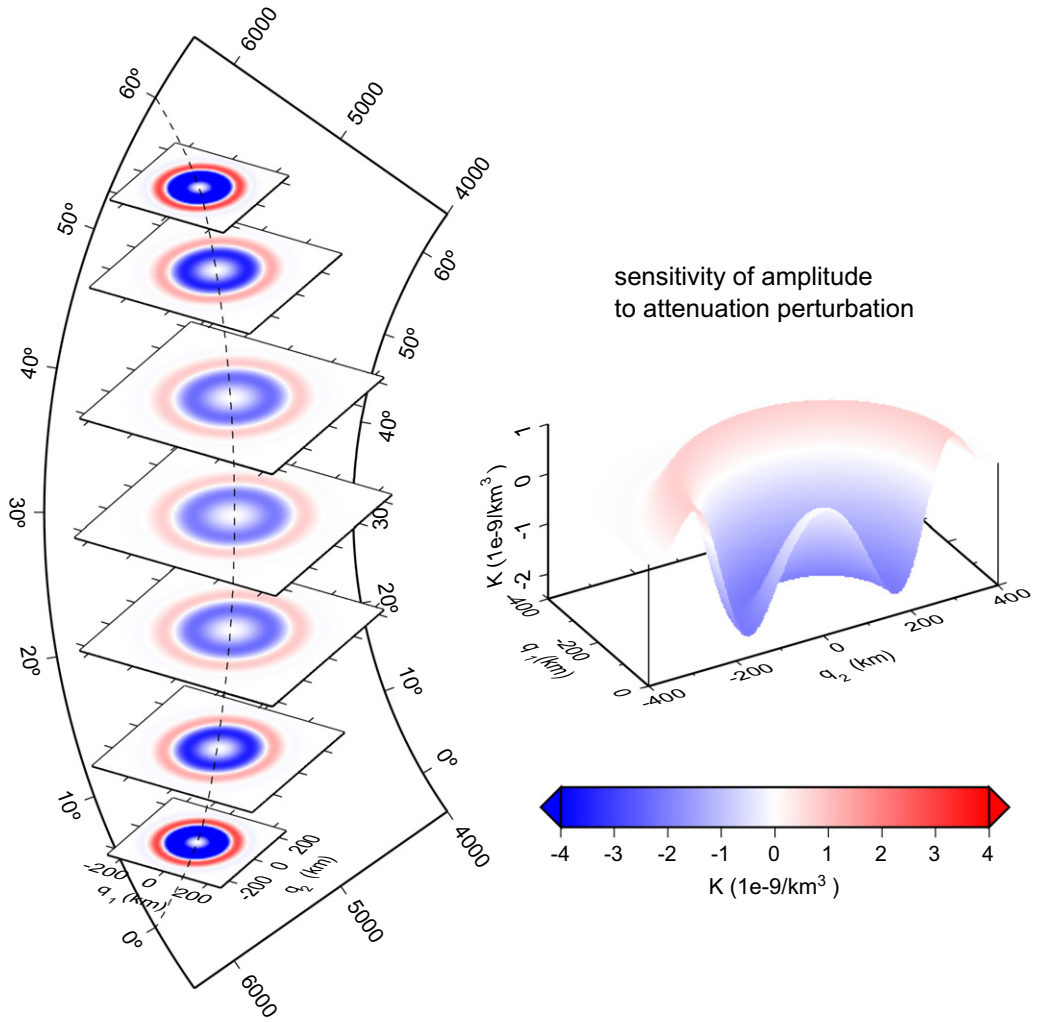

Fig. 6. Amplitude–attenuation sensitivity kernel K_A^Q of a 60° S wave in a spherically symmetric earth, with a dominant period of 10 s. Notations are the same as in Fig. 4.

trade-off between narrowing the band and computational accuracy and efficiency. A practical criterion is that the filter should be wide enough so that $I_{p,k}(\Delta T > \Delta T_{xc})$ is negligible.

4.4. Precision of the kernel quadrature

4.4.1. Designing tests

Much of the gain in efficiency is obtained by designing the kernel integration to be fast with errors allowed as large as, but not exceeding, a few percent (say, 0.03). There are several ways to test the integration precision. All are based on the notion that for very long wavelength model perturbations of very small amplitude, ray theory should be equally valid as first order Born theory. Since the kernel itself is independent of the amplitude and shape of $\delta c/c$ or $\delta Q^{-1}/Q^{-1}$, the quadrature for such small perturbations should revert to the ray-theoretical result. This leads to the following tests:

(1) K_T^c. For a constant velocity perturbation $\delta c/c = \epsilon \to 0$:

$$T + \delta T = \int \frac{\mathrm{d}l}{c + \delta c} \approx \int (1 - \epsilon)\frac{\mathrm{d}l}{c} = T - \epsilon T,$$

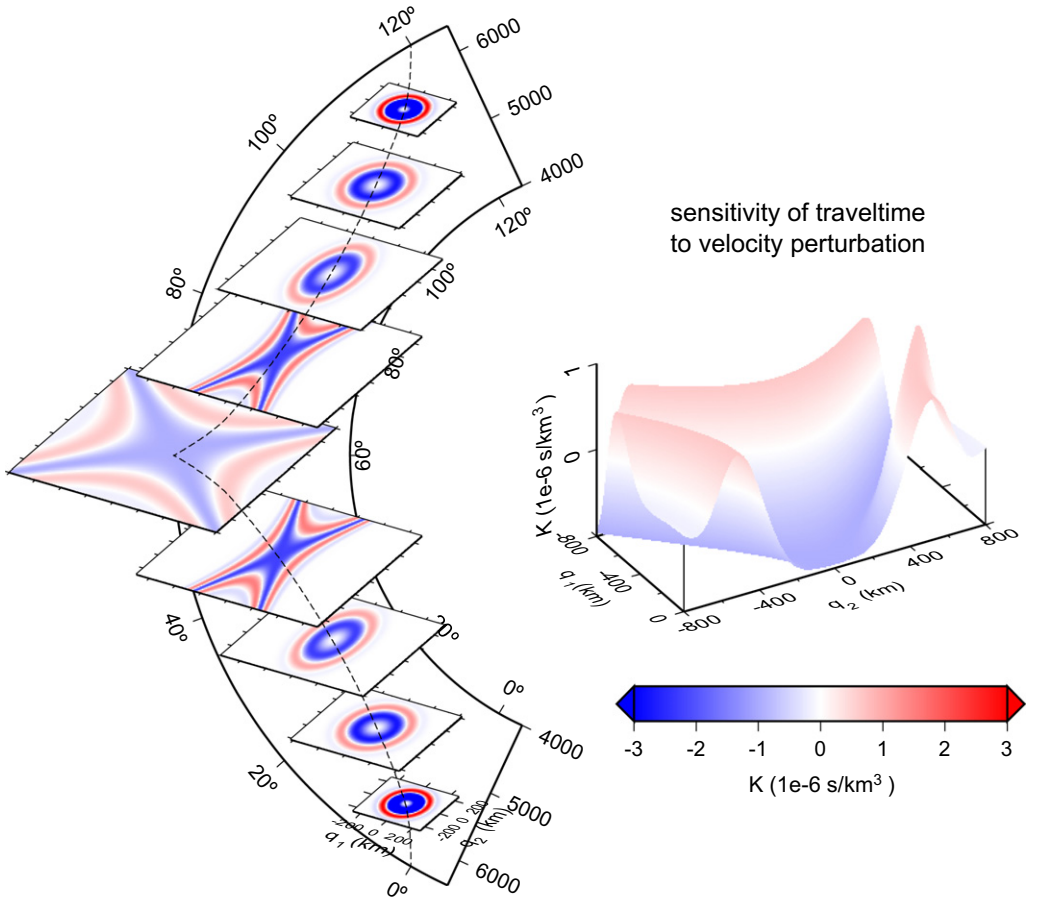

Fig. 7. Traveltime–velocity sensitivity kernel K_T^c of a 120° *SS* wave in a spherically symmetric earth, with a dominant period of 10 s. *Left*: Dashed line is the geometrical ray. Radius (in km) and epicentral distance (in deg) are denoted. The planes are cross-sections *perpendicular* to the ray at 5°, 15°, 30°, 45°, 60°, 75°, 90°, 105°, and 115° respectively, represented in ray centered coordinates (q_1, q_2) (Fig. 1). *Right*: 3D view of the cross-section at 60°. Note that only negative q_1 is plotted.

thus $\delta T = -\epsilon T$. On the other hand, $\delta T = \epsilon \int K_T^c \, \mathrm{d}^3\boldsymbol{r}$. Therefore

$$I_{T1} \equiv \int K_T^c \, \mathrm{d}^3\boldsymbol{r} = \sum_j A_{ij} = -T.$$

In addition, under the assumption of large scale of $\delta c/c$ the integral of K_T^c over a disk S perpendicular to the ray satisfies [4]

$$I_{T2} \equiv \int_S K_T^c \, \mathrm{d}^2\boldsymbol{r} = -\frac{1}{c},$$

where c is the velocity on the ray. Using these results, we define two relative quadrature error estimates of K_T^c:

$$e_{T1} = |I_{T1}/T + 1|, \qquad e_{T2} = |cI_{T2} + 1|. \tag{22}$$

Whereas e_{T1} is global, e_{T2} is local and can be followed along the ray.

(2) K_A^c. A constant velocity perturbation $\delta c/c$ does not affect the focusing/defocusing of rays, so $\delta A = 0$. On the other hand, $\delta A/A = \int K_A^c(\delta c/c) \, \mathrm{d}^3\boldsymbol{r}$. Therefore

$$I_{A1} \equiv \int K_A^c \, \mathrm{d}^3\boldsymbol{r} = \sum_j A_{ij} = 0.$$

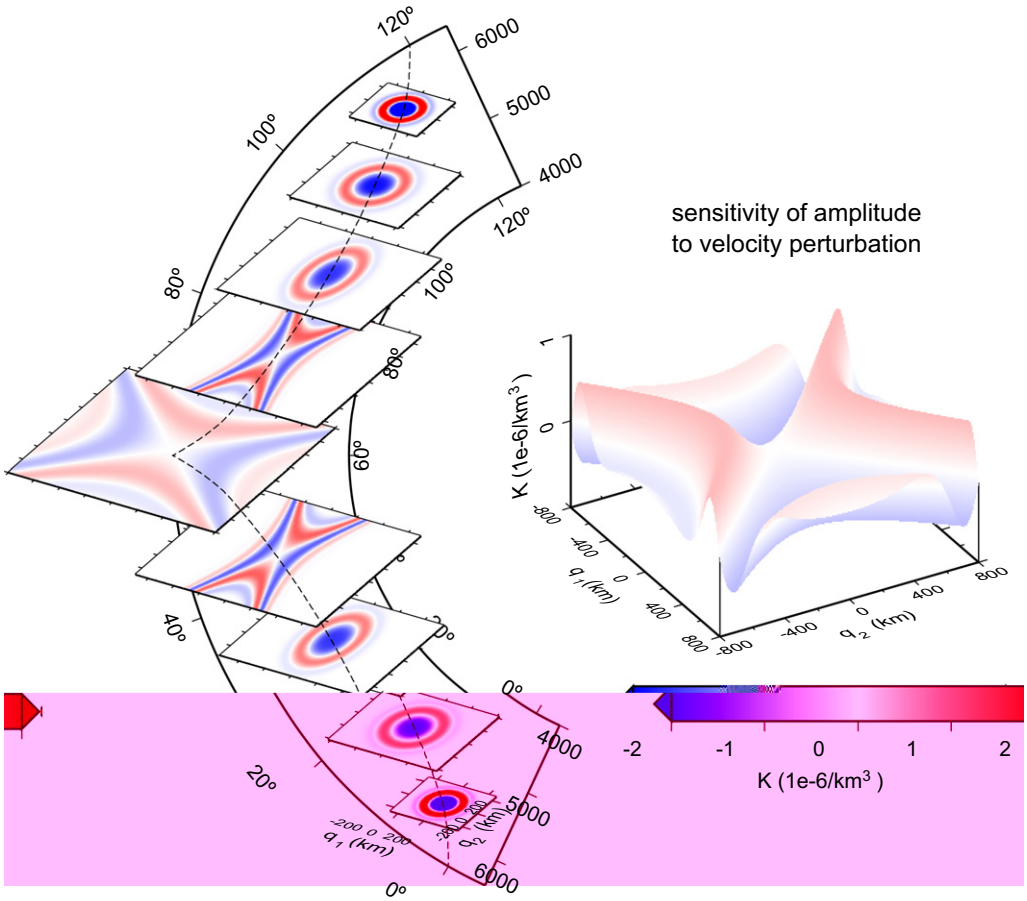

Fig. 8. Amplitude–velocity sensitivity kernel K_A^c of a 120° *SS* wave in a spherically symmetric earth, with a dominant period of 10 s. Notations are the same as in Fig. 7. Note that both positive and negative q_1 is plotted.

Since this has to be the case over every sub-interval on the ray, the integral of K_A^c over a disk S perpendicular to the ray satisfies

$$I_{A2} \equiv \int_S K_A^c \, \mathrm{d}^2\boldsymbol{r} = 0.$$

Using these results, we define two relative quadrature error estimates of K_A^c, the first one global and the second one local:

$$e_{A1} = \left|I_{A1}^-/I_{A1}^+ + 1\right|, \qquad e_{A2} = \left|I_{A2}^-/I_{A2}^+ + 1\right|, \tag{23}$$

where + and − represent quadratures over subdomains where the integrand is positive and negative, respectively.

(3) K_A^Q. Following Dahlen et al. [4], it can be shown that under the assumption of large scale of $\delta Q^{-1}/Q^{-1}$, there are (Appendix A):

$$I_{Q1} \equiv \int K_A^Q \, \mathrm{d}^3\boldsymbol{r} = \sum_j A_{ij} = -\frac{\bar{\omega} t^*}{2},$$

$$I_{A2} \equiv \int_S K_A^Q \, \mathrm{d}^2\boldsymbol{r} = -\frac{\bar{\omega} Q^{-1}}{2c},$$

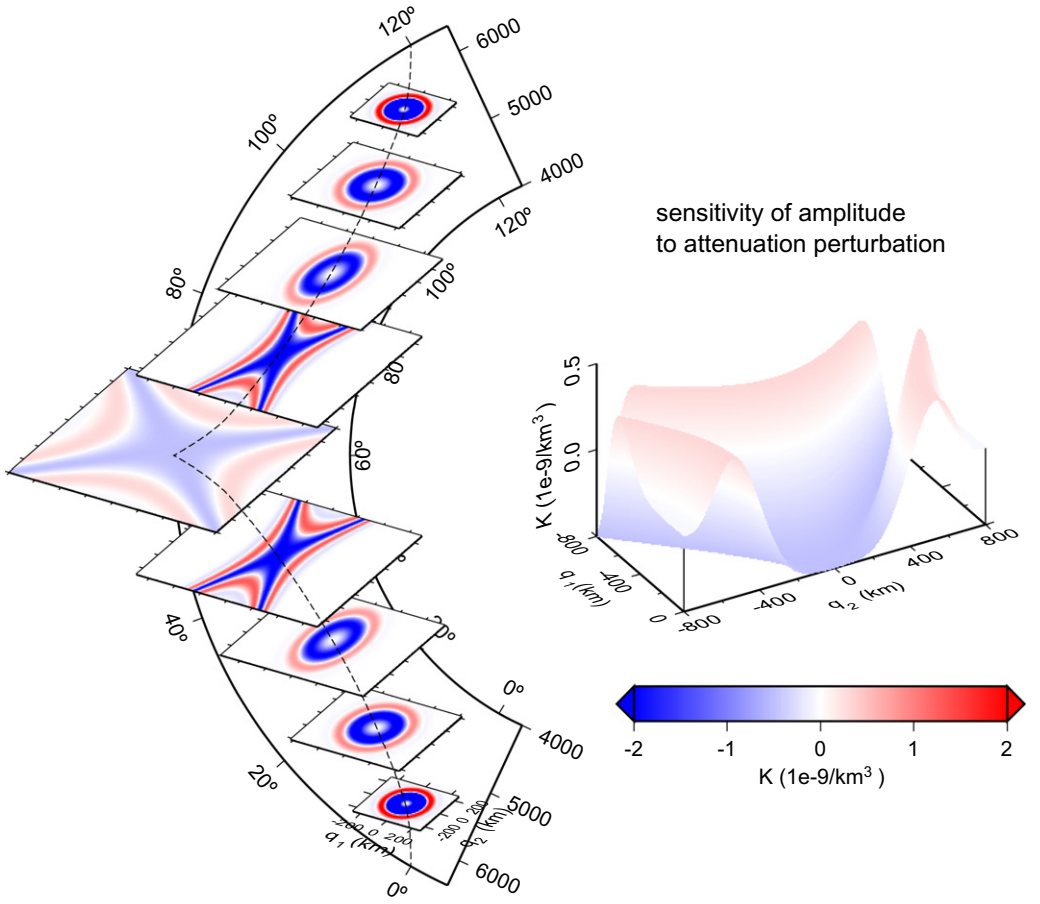

Fig. 9. Amplitude–attenuation sensitivity kernel K_A^Q of a 120° *SS* wave in a spherically symmetric earth, with a dominant period of 10 s. Notations are the same as in Fig. 7. Note that only negative q_1 is plotted.

where $\bar{\omega}$ is defined by (19), $t^* = \int Q^{-1}\,\mathrm{d}l/c$, and c, Q are the velocity and quality factor on the ray, S represents a disk perpendicular to the ray. Using these results, we define two relative quadrature error estimates of K_A^Q, the first one global and the second one local:

$$e_{Q1} = \left|\frac{2I_{Q1}}{\bar{\omega}t^*} + 1\right|, \qquad e_{Q2} = \left|\frac{2cI_{Q2}}{\bar{\omega}Q^{-1}} + 1\right|. \tag{24}$$

We note that these tests include the effects of errors in the frequency integrals as well as in the factors resulting from the dynamic ray tracing, and the limitations of the paraxial approximation. In earlier research (Paper I), we found that the numerical errors of Hessian matrices are generally somewhat larger for *S* waves than for *P* waves. Therefore, we perform tests on the 'worst case', i.e., on shear waves.

4.4.2. Testing results

Fig. 12 shows $e_{T1}, e_{T2}, e_{A1}, e_{A2}, e_{Q1}, e_{Q2}$ for three frequency bands. For *S* waves (Fig. 12a–c), all computational errors are well below typical data standard deviations of 10%. We can also see that disk integration errors e_{T2}, e_{A2}, e_{Q2} are almost the same for different bands. The K_A^c volume integration error e_{A1} is largest for the shortest period, probably due to the rapid oscillation of the kernel w.r.t. ΔT. For *SS* waves (Fig. 12d–f), the best traveltime uncertainties are of the order of 1 s, well above the quadrature precision, even for the longest period of 24 s. Amplitude kernel quadrature errors are equally acceptable.

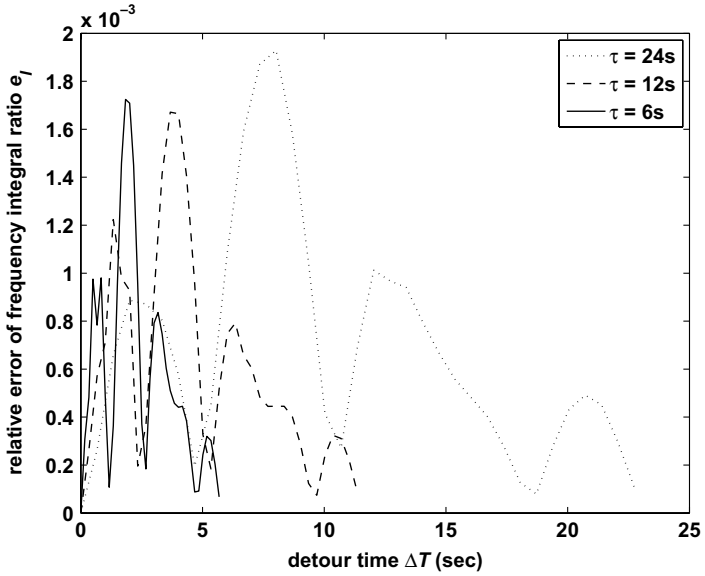

Fig. 10. Relative numerical error of the frequency integral ratio e_I defined by (21) versus detour time, for the spectrum given in (20). The three curves correspond to three bands with dominant periods of $\tau = 24$, 12, 6 s respectively. Each of the curves spans the interval $[0, \Delta T_{\text{lim}}]$.

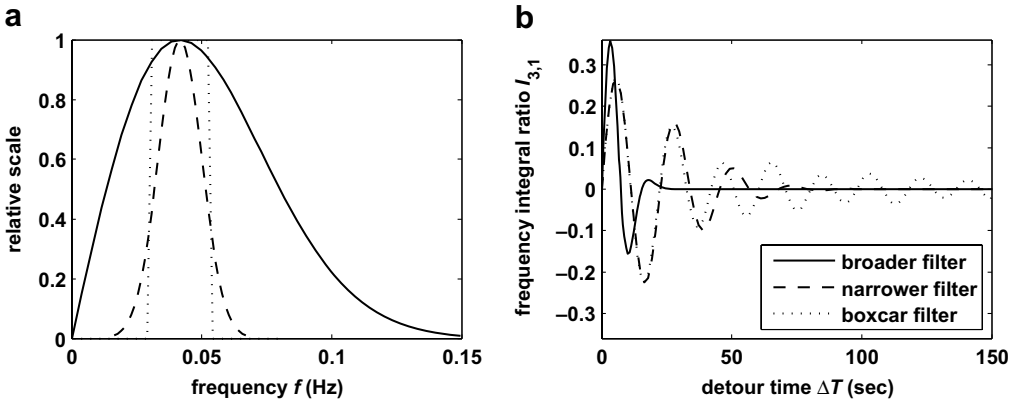

Fig. 11. Influence of filters. (a) Relative amplitude spectra $|\dot{m}(\omega)|$ of three filters: broader and Gaussian in time domain defined by (20) (solid line), narrower and Gaussian in frequency domain (dashed line), narrower and boxcar in frequency domain (dotted line). All three filters have dominant periods $\tau = 24$ s. (b) Frequency integral ratio $I_{p,k}$ in (9) versus detour time, with $p = 3, k = 1$ for S wave traveltime kernels.

A closer inspection of Fig. 12, however, shows a rather complicated behavior of SS errors near and in between the two caustics. With some experimenting, we found that the two error spikes for $\tau = 6$ s can be removed by decreasing the disk integration step size $\mathrm{d}\rho$ in (15), or by increasing the radius r_0 of the sphere V_0 around a caustic (Section 3.4). This indicates that these very localized errors are a consequence of the singular behavior of the kernels near a caustic. This problem is more benign at longer periods where the kernel changes more gradually.

This is not true for another type of error: for the longest period, K_T^c, K_A^c, K_A^Q all have large disk integration errors between two caustics. This is where the Hessian element H_{11} becomes negative (Paper I), and the kernel shape becomes hyperbolic instead of elliptical or circular. Along the asymptotes of this hyperbola, the detour time remains zero, independent of the distance to the ray. By imposing a finite integration limit ρ_m (see (13)),

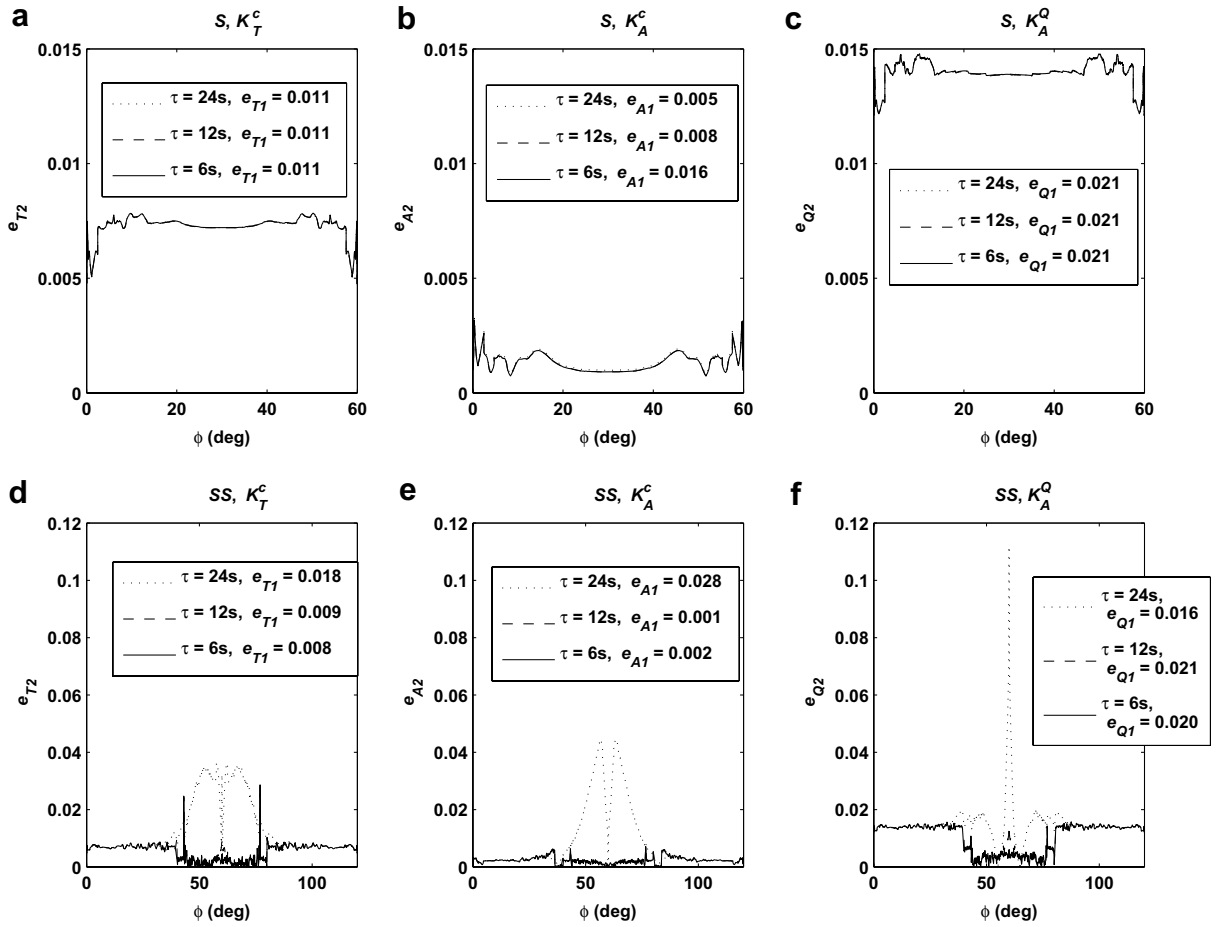

Fig. 12. Kernel disk integration errors e_{T2}, e_{A2}, e_Q

we exclude scatterers of large sensitivity, located outside of the surface of integration. We found that the large errors between caustics can be removed by increasing $\rho_{\lim}$ in (13) to include more scattered waves. This, however, leads soon to unphysical situations because the scatterer is outside of the region where the paraxial approximation is meaningful. This 'hyperbolic problem' is most serious for the longest period, because the longer period wave has a broader kernel and a larger ΔT_m, which makes the first term in (13) exceed $\rho_{\lim}$.

4.5. Effects of epicentral distance on kernel quadrature precision

A similar but more serious precision problem occurs for waves observed near the source antipode. Fig. 13 shows effects of epicentral distance Δ on e_{T1}, e_{A1}, e_{Q1}, and the average e_{T2}, e_{A2}, e_{Q2} over the entire ray. Guided by the results of the last section, we focus on the bands with largest errors, i.e., the shortest period band for S waves and the longest period band for SS waves. For S waves (Fig. 13a), all errors are of the order of a few percent regardless of the epicentral distance. e_{T1}, e_{A1}, e_{Q1} tend to decrease with Δ, which is consistent with the trend of Hessian element errors with Δ (Paper I).

For SS waves (Fig. 13b), kernel integration errors are obviously larger due to the 'hyperbolic problem', but still acceptable for $\Delta \leqslant 140°$. The threshold of 140° depends on the wave period. Errors for $\tau > 24$ sec are larger than in Fig. 13b, but smaller at shorter periods. Beyond 140°, kernel integration errors increase rapidly, again due to the behavior of the kernel in between the two caustics. When Δ is close to 180°, $H_{22} \ll |H_{11}|$,

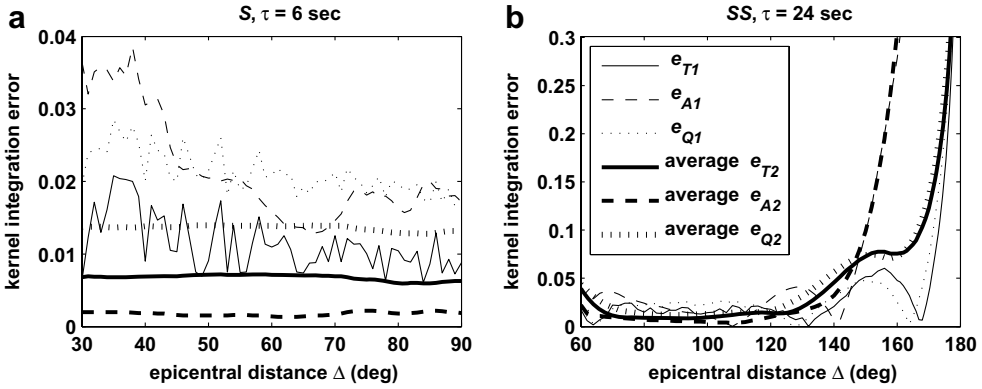

Fig. 13. Kernel integration errors versus epicentral distance for (a) an S wave with a dominant period of 6 s; (b) an SS wave with a dominant period of 24 s. $e_{T1}, e_{T2}, e_{A1}, e_{A2}, e_{Q1}, e_{Q2}$ are defined by (22)–(24). The thick lines depict the average of e_{T2}, e_{A2}, e_{Q2} over the entire ray.

so the hyperbola is strongly flattened, and the region widens alongside the asymptote where $\Delta T \approx 0$. Consequently, the exclusion of the integration surface for $\rho > \rho_m$ has a larger effect. Physically, the error can be understood when we realize that for a station at the antipode, waves departing the source in *all* azimuths arrive at this station: the assumption of equal excitation for direct and scattered waves breaks down; the sensitivity is spread over the whole mantle and the kernel is no longer banana shaped or even localized. Instead, the kernel looks like two hollow cones with one vertex at source and the other vertex at receiver. If data at $\Delta > 140°$ are crucial in the data set, efficient paraxial methods cannot be used, but an alternative method used by Calvet and Chevrot [2], who set up a table of traveltimes and geometrical spreading for sources at every depth and every epicentral distance traveled, may still provide correct de-localized kernels.

4.6. Effects of step size on kernel quadrature precision

Since the CPU time devoted to the computation of the matrix reduces with the third power of the integration step size (or the square of $d\rho$ if it is varied independently from dl), it is important to determine the largest step size that still yields an acceptable precision. Fig. 14 shows the kernel integration error as a function of $d\rho$ (see Fig. 2). Again, we opt for a 'worst case' scenario and select cases with largest errors from last two sections: for S waves, the shortest period band and $\Delta = 35°$; for SS waves, the longest period band and $\Delta = 130°$. The

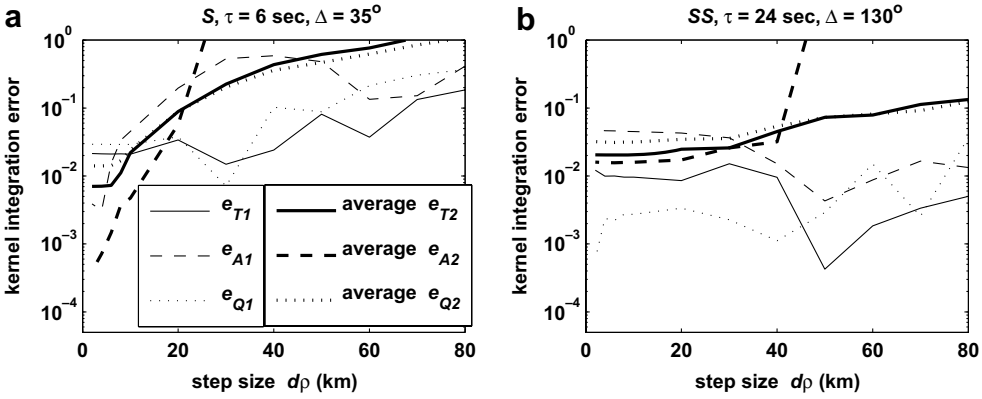

Fig. 14. Kernel integration errors versus disk integration step size $d\rho$ (see Fig. 1) for (a) an S wave with a dominant period of 6 s and epicentral distance of 35°; (b) an SS wave with a dominant period of 24 s and epicentral distance of 130°. $e_{T1}, e_{T2}, e_{A1}, e_{A2}, e_{Q1}, e_{Q2}$ are defined by (22)–(24). The thick lines depict the average of e_{T2}, e_{A2}, e_{Q2} over the entire ray.

small values of e_{T1},e_{A1},e_{Q1} at large $\mathrm{d}\rho$ are a consequence of the cancellation of the rapid positive–negative oscillations of e_{T2}, e_{A2}, e_{Q2} near singular points, so the averages of e_{T2}, e_{A2}, e_{Q2} over the ray are better error estimates. To obtain kernel integration errors of a few percent, which are below typical data uncertainties, the optimum $\mathrm{d}\rho$ is about 10 km for S waves and about 30 km for SS waves. The high errors at larger $\mathrm{d}\rho$ are mainly due to high errors near singular points.

The step size along the ray $\mathrm{d}l$ is determined in the earlier stage of dynamic ray tracing (Paper I). It affects the kernel quadrature precision by affecting the precision of the Hessian elements. The optimum $\mathrm{d}l$ we found in Paper I (about 20 km) is of the same order as the optimum $\mathrm{d}\rho$.

Note that each point in Fig. 14 is produced with a constant $\mathrm{d}\rho$ independent of ray path. The optimum $\mathrm{d}\rho$ obtained in this way represents the minimum $\mathrm{d}\rho$ required along the entire ray path, usually near singular points where the kernel is the thinnest. However, near the center of the ray, the kernel becomes much wider, and using the same minimum $\mathrm{d}\rho$ in this region is obviously very inefficient. In practice, we use a $\mathrm{d}\rho$ dependent on kernel width with an upper limit, as described by (15). This significantly decreases the computational time, for example, by ~56% for the SS wave in Fig. 14b with $\mathrm{d}\rho = 20$ km while obtaining the same precision. In addition, we make $\mathrm{d}\rho$ frequency dependent by using (13)–(15), which further reduces the computational time by a factor approximately equal to the inverse ratio of the dominant periods of different frequency bands.

5. Conclusions

We investigated the quadrature precision for efficient computation of matrix coefficients needed in finite-frequency seismic tomography. Under normal circumstances, acceptable precision is easily obtained for minimum integration step size of 10 km for S waves and 30 km for SS waves. The computational errors are a product of the simple Riemann integration we adopted. For S waves, kernel quadrature precisions are lowest for waves with shortest period, and increase with decreasing epicentral distance. Since much of the error can be traced back to the variation of the integrand within the volume ΔV_P, a polynomial representation of the integrand within each volume element would potentially allow us to increase $\mathrm{d}\rho$ while maintaining precision by solving the integral analytically for each ΔV_P. This, however, is no panacea for another type of error we discovered: For SS waves, kernels become hyperbolic instead of elliptical between two caustics, which makes the paraxial approximation less valid. This can potentially produce large errors. These errors are most pronounced for waves with long periods (>20 s) and near antipodal epicentral distances (>140°). The error at long periods can be kept under control by reverting to ray theory near a singularity. The error at large distances forces us to abandon the paraxial approximation.

Acknowledgements

We thank Ignace Loris for discussion. Yue Tian was supported by the National Science Foundation under grant number EAR0309298.

Appendix A. Designing tests on Q kernel quadrature precision

Following Dahlen et al. [4] (Section 7), we derive the analytical expressions for K_A^Q quadrature precision tests. Using (8), rewrite (6) as

$$K_A^Q = -\frac{Q^{-1}}{4\pi c}\sqrt{|\det(\boldsymbol{H})|}\,\frac{\int_0^\infty \omega^2 |\dot{m}(\omega)|^2 \sin\Theta\,\mathrm{d}\omega}{\int_0^\infty |\dot{m}(\omega)|^2\,\mathrm{d}\omega},$$

where $\Theta = \omega\Delta T - \Delta\Phi$. In ray centered coordinates (l, q_1, q_2), a surface element in the q_1–q_2 plane (Fig. 1) is $\mathrm{d}S = (1 + \sum_i q_i \partial c/\partial q_i)\,\mathrm{d}q_1\,\mathrm{d}q_2$. We integrate K_A^Q over a disk S perpendicular to the ray

$$I_{Q2} \equiv \int_S K_A^Q\,\mathrm{d}S = -\frac{1}{4\pi}\int_S \mathrm{d}q_1\,\mathrm{d}q_2\left(1 + \sum_i q_i \frac{\partial c}{\partial q_i}\right)\frac{Q^{-1}}{c}\sqrt{|\det(\boldsymbol{H})|}\,\frac{\int_0^\infty \omega^2 |\dot{m}(\omega)|^2 \sin\Theta\,\mathrm{d}\omega}{\int_0^\infty |\dot{m}(\omega)|^2\,\mathrm{d}\omega}. \tag{25}$$

In practice, S is limited to the region where K_A^Q has an appreciable amplitude. If the lateral scale of $\delta Q^{-1}/Q^{-1}$ is much larger than the seismic wavelength, $\partial c/\partial q_i \approx 0$ and Q^{-1}, c can be approximated by their values on the ray. Hence

$$I_{Q2} = -\frac{1}{4\pi}\frac{Q^{-1}}{c}\bigg|_{(l,0,0)} \frac{\int_0^\infty \mathrm{d}\omega\omega^2 |\dot{m}(\omega)|^2 \sqrt{|\det(\boldsymbol{H})|}\int_S \sin\Theta\,\mathrm{d}q_1\,\mathrm{d}q_2}{\int_0^\infty |\dot{m}(\omega)|^2\,\mathrm{d}\omega}.$$

Using the Gaussian integral identity $\int_S \sin\Theta\,\mathrm{d}q_1\,\mathrm{d}q_2 = 2\pi/(\omega\sqrt{|\det(\boldsymbol{H})|})$, we get

$$I_{Q2} = -\frac{\bar{\omega}}{2}\cdot\frac{Q^{-1}}{c}\bigg|_{(l,0,0)},$$

where $\bar{\omega}$ is defined by (19). Thus, we have obtained (19) and the second equation of (24). To derive the 1st equation of (24), we only need to integrate I_{Q2} along the ray (ray length L):

$$I_{Q1} = \int_0^L I_{Q2}\,\mathrm{d}l = -\frac{\bar{\omega}}{2}\int_0^L \frac{Q^{-1}}{c}\,\mathrm{d}l = -\frac{\bar{\omega}t^*}{2}.$$

References

[1] C.B. Barber, D.P. Dobkin, H.T. Huhdanpaa, The Quickhull algorithm for convex hulls, ACM Trans. Math. Softw. 22 (1996) 469–483.
[2] M. Calvet, S. Chevrot, Traveltime sensitivity kernels for PKP phases in the mantle, Phys. Earth Planet. Inter. 153 (2005) 21–31.
[3] F.A. Dahlen, A.M. Baig, Fréchet kernels for body-wave amplitudes, Geophys. J. Int. 150 (2002) 440–466.
[4] F.A. Dahlen, S.-H. Hung, G. Nolet, Fréchet kernels for finite-frequency traveltimes—I. Theory, Geophys. J. Int. 141 (2000) 157–174.
[5] N. Favier, S. Chevrot, Sensitivity kernels for shear wave splitting in transverse isotropic media, Geophys. J. Int. 153 (2003) 213–228.
[6] N. Favier, S. Chevrot, D. Komatitsch, Near-field influence on shear wave splitting and traveltime sensitivity kernels, Geophys. J. Int. 156 (2004) 467–482.
[7] S.-H. Hung, F.A. Dahlen, G. Nolet, Fréchet kernels for finite-frequency traveltimes—II. Examples, Geophys. J. Int. 141 (2000) 175–203.
[8] S.-H. Hung, F.A. Dahlen, G. Nolet, Wavefront healing: a banana-doughnut perspective, Geophys. J. Int. 146 (2001) 289–312.
[9] W. Menke, Case studies of seismic tomography and earthquake location in a regional context, in: A. Levander, G. Nolet (Eds.), Seismic Earth: Array analysis of broadband seismograms, AGU Monograph Ser., 2005, pp. 7–36.
[10] R. Montelli, G. Nolet, F.A. Dahlen, G. Masters, A catalogue of deep mantle plumes: new results from finite-frequency tomography, Geochem. Geophys. Geosyst. 7 (Q11007) (2006), doi:10.1029/2006GC001248.
[11] R. Montelli, G. Nolet, F.A. Dahlen, G. Masters, E.R. Engdahl, S.-H. Hung, Finite-frequency tomography reveals a variety of plumes in the mantle, Science 303 (2004) 338–343.
[12] R. Montelli, G. Nolet, G. Masters, F.A. Dahlen, S.-H. Hung, Global P and PP traveltime tomography: rays versus waves, Geophys. J. Int. 158 (2004) 637–654.
[13] G. Nolet, A Breviary of Seismic Tomography, CUP, Cambridge, UK, in press.
[14] G. Nolet, R. Montelli, Optimal parameterization of tomographic models, Geophys. J. Int. 161 (2005) 1–8.
[15] J. Ritsema, L.A. Rivera, D. Komatitsch, J. Tromp, H.-J. van Heijst, Effects of crust and mantle heterogeneity on pp/p and ss/s amplitude ratios, Geophys. Res. Lett. 29 (2002), doi:10.1029/2001GL013831.
[16] M. Sambridge, J. Braum, H. McQueen, Geophysical parameterization and interpolation of irregular data using natural neighbours, Geophys. J. Int. 122 (1995) 837–857.
[17] M. Sambridge, O. Gudmundsson, Tomographic systems of equations with irregular cells, J. Geophys. Res. 103 (1998) 773–781.
[18] Y. Tian, S.-H. Hung, G. Nolet, R. Montelli, F.A. Dahlen, Dynamic ray tracing and traveltime corrections for global seismic tomography, J. Comput. Phys. in press.
[19] V. Červený, F. Hron, The ray series method and dynamic ray tracing systems for 3-D inhomogeneous media, Bull. Seis. Soc. Am. 70 (1980) 47–77.